



## ISTITUTO NAZIONALE DI RICERCA METROLOGICA Repository Istituzionale

### On-Chip Magnetic Platform for Single-Particle Manipulation with Integrated Electrical Feedback

This is the author's accepted version of the contribution published as:

*Original*

On-Chip Magnetic Platform for Single-Particle Manipulation with Integrated Electrical Feedback / Monticelli, Marco; Torti, Andrea; Cantoni, Matteo; Petti, Daniela; Albisetti, Edoardo; Manzin, Alessandra; Guerriero, Erica; Sordan, Roman; Gervasoni, Giacomo; Carminati, Marco; Ferrari, Giorgio; Sampietro, Marco; Bertacco, Riccardo. - In: SMALL. - ISSN 1613-6810. - 12:7(2016), pp. 921-9-929. [10.1002/sml.201500916]

*Availability:*

This version is available at: 11696/54650 since: 2021-02-20T22:43:02Z

*Publisher:*

Wiley

*Published*

DOI:10.1002/sml.201500916

*Terms of use:*

This article is made available under terms and conditions as specified in the corresponding bibliographic description in the repository

*Publisher copyright*

WILEY

This article may be used for non-commercial purposes in accordance with Wiley Terms and Conditions for Use of Self-Archived Versions

(Article begins on next page)

DOI: 10.1002/ ((please add manuscript number))

Article type: Full Paper

## On-chip magnetic platform for single particle manipulation with integrated electrical feedback

*Marco Monticelli<sup>\*</sup>, Andrea Torti, Matteo Cantoni, Daniela Petti<sup>\*</sup>, Edoardo Albisetti, Alessandra Manzin, Erica Guerriero, Roman Sordan, Giacomo Gervasoni, Marco Carminati, Giorgio Ferrari, Marco Sampietro and Riccardo Bertacco*

M. Monticelli, Dr. A. Torti, Prof. M. Cantoni, Dr. D. Petti, Dr. E. Albisetti and Prof. R. Bertacco

Polifab center, Physics Department, Politecnico di Milano, Via G. Colombo n.81, zip code: 20133, Milan, Italy

E-mail: marco.monticelli@polimi.it, daniela.petti@polimi.it

Dr. A. Manzin,

INRIM (Istituto Nazionale di Ricerca Metrologica), Strada delle Cacce n. 91, zip code: 10135, Turin, Italy

Dr. E. Guerriero and Prof. R. Sordan,

L-NESS center, Physics Department, Politecnico di Milano, Via Anzani n.42, zip code: 22100, Italy

G. Gervasoni, Dr. M. Carminati, Dr. G. Ferrari and Prof. M. Sampietro

Polifab center, Electronics Department, Politecnico di Milano, P.zza Leonardo da Vinci n.32, zip code: 20133, Italy

Keywords: Magnetic beads, Magnetic sensors, Anisotropic magnetoresistance, Magnetic tweezers, Lab-on-chip.

Methods for the manipulation of single magnetic particles have become of particular interest for in-vitro biological studies. Most of them require an external microscope to provide the operator with the feedback for controlling the particle motion, thus preventing their use in high throughput experiments. In this paper, a simple and compact system with integrated electrical feedback is presented, implementing in the very same device both the manipulation and the detection of single particles transit. The proposed platform is based on zig-zag shaped magnetic nanostructures, where transverse magnetic domain walls are pinned at the corners and attract magnetic particles in suspension. By applying suitable external magnetic fields, domain walls move to the nearest corner, thus causing the step by step displacement of the particles along the nanostructure. The very same structure is employed also for detecting the bead transit. Indeed, the presence of the magnetic particle over the domain wall affects the depinning field required for its displacement. This characteristic field can be monitored

through anisotropic magnetoresistance measurements, thus implementing an integrated electrical feedback of the bead transit. In particular, the individual manipulation and detection of single 1  $\mu\text{m}$  sized beads is here demonstrated.

## 1. Introduction

In the last years, the use of magnetic micro- and nano-particles in lab-on-chip devices has attracted a growing interest in the fields of biology and nanomedicine. Nowadays, functionalized magnetic particles are widely employed as carriers and labels for cell and molecular manipulation,<sup>[1,2]</sup> drug delivery,<sup>[3,4]</sup> sample preparation and biosensing.<sup>[5,6,7]</sup> Several technologies have been developed to capture and manipulate with high resolution particles suspended in a biological medium. In particular, magnetic manipulators<sup>[8,9,10,11]</sup> have proved to be very effective tools, even compared with competing technologies such as electrophoresis and optical tweezers, because magnetic fields are not screened by biological environments and are non-invasive for cells and biomolecules. This is particularly true for systems not exploiting current-carrying wires in direct contact with biological entities, thus avoiding localized Joule heating. Arrays of magnetic elements patterned on-chip have been proposed for the transport of single magnetic particles by exploiting their capability of focusing external magnetic fields.<sup>[12,13]</sup> In addition, it has been shown that magnetic domain walls (DWs) in a ferromagnetic thin film can be used to manipulate magnetic particles at a solid-fluid interface.<sup>[14,15]</sup> In this context, an innovative magnetic handling technology, called "Domain wall Tweezers" (DWT),<sup>[16]</sup> has been proposed by some of the authors. This platform is based on the controlled displacement of constrained DWs in ferromagnetic conduits, allowing for the manipulation of magnetic micro and nanoparticles with resolution down to 100 nm.<sup>[17]</sup> In all these works, however, the accurate bead manipulation is performed by the operator monitoring the motion via an optical microscope, thus preventing their application to some relevant cases, such as high-throughput biological experiments and automatized microfluidics platforms for lab-on-chip devices.

As regards biological applications, nowadays there is an emerging need of platforms allowing for the investigation of the controlled interaction between individual particles and biological entities, well beyond conventional studies on populations of cells randomly interacting with particles in solution. In this scenario, magnetic manipulation systems offer unique opportunities for the non-invasive synchronization of the stimulus and the observation, as well as for tuning the strength of the mechanical interaction.<sup>[18]</sup> In order to put any result on a solid statistical basis, however, currently available technologies would require to perform several

sequential and time consuming experiments. A typical example is in-vitro drug delivery testing, which represents a fundamental step for preliminary studies on the effect of drugs on biological model systems.<sup>[19]</sup> Remotely controlled systems, for high throughput and automatic delivery to cells of single magnetic beads loaded with drugs, are required to perform parallel experiments on individual cells. In the context of microfluidics, new paradigms based on the motion of discrete quantities of reagents are emerging, such as the so called “droplet microfluidics”. By analogy, magnetophoretic systems could be used to implement a “bead microfluidics”, where single beads act as carriers moving along pre-defined paths, while visiting different chemical environments. However, currently available manipulation technology should be complemented with integrated methods for bead transit detection, in order to realize automatized microfluidic systems suitable for miniaturized lab-on-chip devices. For both applications, the development of a closed-loop control system, based on integrated sensors providing the necessary feedback on the motion of each particle, is a fundamental prerequisite.

Different approaches can be envisaged for the integrated detection of magnetic particles, exploiting magnetic sensors based on anisotropic magnetoresistance (AMR),<sup>[20]</sup> giant magnetoresistance (GMR),<sup>[21]</sup> tunneling magnetoresistance (TMR)<sup>[22]</sup> and Hall effect.<sup>[23]</sup> Recently, on-chip magnetic tweezers based on current lines have been combined with GMR<sup>[24]</sup> and AMR<sup>[25]</sup> sensors, to achieve manipulation and detection of magnetic beads.<sup>[26]</sup> However, these systems are quite complex as they require the integration of distinct devices implementing particle sensing and manipulation. Another approach has been proposed by Rapoport et al.<sup>[27]</sup>, where the magneto-mechanical sensing of particles is employed in conjunction with the use of magnetic conduits for transport. In this case, however, the particle detection has been demonstrated only using external optical elements, while an integrated detection system based on GMR has been only foreseen. Other groups have proposed the use of CMOS sensors for capacitive detection of beads locally manipulated by micro-coils,<sup>[28]</sup> but long distance transport is not reported and the capacitive detection poses serious constraints for the use in microfluidics system with conductive solutions. In this paper, we present an innovative on-chip technology allowing to overcome these difficulties thanks to the integration of both the manipulation and sensing functionalities within the very same magnetic nanostructure. A zig-zag shaped magnetic conduit is used for the manipulation of individual magnetic particles bound to constrained domain walls, which move from a corner to the next one upon the application of suitable magnetic fields. The detection of the particle transit through a peculiar corner is performed by exploiting a method for single particle

detection based on AMR measurements, previously introduced for Permalloy micron-sized square rings<sup>[29]</sup> and nanometric L-shaped sensors.<sup>[30]</sup> The presence of the magnetic particle over the domain wall affects its depinning field, which is the minimum magnetic field required for moving the domain wall from one corner to the following one. Thanks to the AMR effect, this characteristic field can be monitored by recording the voltage drop across a specific corner flanked by two electrodes during a fast sweep of the magnetic field, so that the transit of a bare DW can be distinguished from that of a DW bound to a magnetic particle. This implements the desired integrated feedback in a compact device suitable to perform, at the same time, both the fine control and the detection of the motion of a single particle in a liquid environment. In particular, here we demonstrate the simultaneous manipulation and detection of a 1  $\mu\text{m}$  sized magnetic bead (commercial MyOne®-Dynabeads) and we show, through micromagnetic simulations, that this system can be used also with smaller particles, down to about 100 nm diameter. The advantages with respect to competing magnetic technologies can be summarized as follows: (i) multiple functionalities can be integrated within the very same magnetic nanostructure made of a single layer of Permalloy, i.e. transport, detection and sorting, (ii) a fully integrated on-chip magnetic detection of beads is performed, without need of external optical components or distinct complex magnetic sensors. The addition of such electrical feedback on the particle motion to the magnetic domain wall tweezers technology represents a fundamental achievement in view of novel closed-loop microfluidic platforms.

## 2. Results and Discussion

A picture of the experimental setup is shown in **Figure 1a-b**. A 3x3 cm<sup>2</sup> silicon chip comprising six nanofabricated devices is wire-bonded to an interconnection board for electrical measurements. As shown in panel b, a simple polydimethylsiloxane (PDMS) microfluidic chamber is sealed on top of the chip to contain the liquid with the beads in suspension. For performing the bead manipulation, an external magnetic field is applied by means of a quadrupole electromagnet (not shown). The layout of a single device is shown in Figure 1c-d. It consists of a 30 nm thick and 200 nm wide zig-zag shaped conduit of Permalloy (Ni<sub>80</sub>Fe<sub>20</sub>), where the length of each segment is 2  $\mu\text{m}$ . A 600 nm-wide injector pad is located at the beginning of the structure to allow the nucleation of a single DW suitable for particles manipulation. The very same conduit is equipped with four gold contacts (1-4 in the panel c of Figure 1), allowing 4-wire measurements: the external leads 1-4 are used for injecting the current, while the internal contacts 2-3 are used to measure the voltage drop across the corner.

The working principle of the platform is sketched in **Figure 2**, reporting the micromagnetic configurations induced in the conduit during operation, as calculated with OOMMF (Object Oriented MicroMagnetic Framework).<sup>[31]</sup> A single DW can be injected and displaced from corner to corner, in the magnetic zig-zag, by applying a sequence of magnetic field pulses.<sup>[2,17]</sup> First, the structure is initialized by a field  $H_0=1000$  Oe along the negative direction of the x-axis (see the sketch in Figure 1d), leading to a single domain micromagnetic configuration (see Figure 2a) **according to a procedure previously optimized.**<sup>[17]</sup> The application of a pulse field  $H_1=150$  Oe, at 15 degrees with respect to the positive direction of the x-axis, nucleates a single head-to-head DW by reversing the magnetization of the injection pad and propagating the DW up to the first corner in the zig-zag. The DW position remains stable after removal of  $H_1$ , due to the pinning potential at the corner (see Figure 2b). This is the initial position at which the stray field from the DW captures a magnetic particle in suspension. The DW can be then moved along the conduit up to the last corner of the conveyor, with a sequence of external magnetic field pulses ( $H_2 = 190$  Oe) at  $\pm 45$  degrees with respect to the x-direction, i.e., along the segments direction (see Figure 2c). The single bead initially captured by the DW follows the DW motion, moving from one corner to the next one with a stepping motion. In this case the field required for the displacement of both the DW and the bead is slightly higher than in case of the single DW. This difference allows to distinguish the transit of the particle from that of the bare domain wall, through AMR.

The use of AMR for the detection of a DW at a given corner is illustrated in Figure 2b-d. To this scope, a corner of the conduit is provided with two contacts (leads 2-3) to measure the local voltage drop associated to the current flowing through the conduit from 1 to 4. When a transverse Néel DW (see the OOMMF simulations of Figure 2a-c) is placed between the sensing contacts, the current density  $\mathbf{J}$  and the magnetization  $\mathbf{M}$  become locally perpendicular. Due to the AMR effect, the resistivity of the conduit between leads 2-3, in presence of the DW ( $\rho_L$  in Figure 2c) decreases compared to the case in which the DW is absent ( $\rho_H$  in Figure 2a-b). Therefore, the displacement of the DW away from or towards the corner and its associated depinning field can be easily read electrically, by monitoring the voltage drop between leads 2 and 3 ( $V_{AMR}$ ) at constant current.

As introduced above, the possibility of distinguishing the transit of the single DW from that of a magnetic bead bound to the DW relies on the fact that the presence of a superparamagnetic bead affects the value of the depinning field ( $H_{dep}$ ) of the DW. As schematically illustrated in Figure 2d, when a magnetic field ( $H_S$ ) is applied to displace the DW, the bead magnetic moment  $\mu$  creates a stray field which opposes the external field, causing an increase of the

field  $H_{\text{dep}}$  required to move the DW. This can be measured with high accuracy, by monitoring the AMR signal  $V_{\text{AMR}}$  (i.e. the voltage drop between 2 and 3) as a function of the magnetic field. In order to estimate the expected variation of the depinning field due to the presence of the bead and the entity of the AMR response, the system has been modeled by assuming a negligible interaction of the current on the micromagnetic configuration. Specifically, the modeling approach couples a micromagnetic solver,<sup>[32]</sup> for the determination of the magnetic domain states, with a magnetotransport model, for the calculation of the current path.<sup>[33]</sup> The AMR effect is modeled according to Refs. [34], [35] by solving the transport equation with a finite element method. The simulated voltage drop due to AMR (normalized to the baseline  $V_0$  calculated for the initial configuration shown in Figure 2c) as function of the external magnetic field is illustrated in Figure 2e. It refers to a DW moving away from the measurement corner, while dragging a 1  $\mu\text{m}$  bead in suspension with its surface located 40 nm above the conduit (red curve) or free of it (black curve). The depinning field is the field at which the transition between the two resistance states occurs, corresponding to a step in the graph of Figure 2e. From simulations, the variation of the depinning field ( $\Delta H_{\text{dep}}$ ) due to the presence of a bead results 13 Oe. An uncertainty of  $\pm 3$  Oe on this value takes into account the possible deviation of the nanostructure width ( $\pm 15$  nm) from the nominal value, a maximum misalignment of the external field of  $\pm 2$  degrees (according to the experimental uncertainty), stochastic effects due to thermal agitation at room temperature (estimated in the micromagnetic simulations by means of a Langevin approach<sup>[36]</sup>), a spread of the bead magnetic moment of  $\pm 10\%$  and an uncertainty on the bead position of  $\pm 15$  nm, both out-of-plane and along the corner diagonal. In simulations, the bead centre is placed close to the external edge of the nanostructure corner. As a matter of fact, the bead is not located above the geometrical centre of the corner, but it is slightly displaced towards the edge of the nanostructure, when an external magnetic field ( $H_{\text{ext}}$ ) comparable with the depinning field is applied. This is evident from the optical microscopy image in the inset of **Figure 3** and confirmed by numerical simulations performed with OOMMF. The magnetic potential energy of a superparamagnetic bead (1  $\mu\text{m}$  diameter, susceptibility  $\chi = 1.43$ ), attracted by a DW in a zig-zag shaped conduit is calculated for an external magnetic field ( $H_{\text{ext}}$ ) of 195 Oe applied along one zig-zag segment (see Figure 3), according to the following equation:

$$U_{\text{mag}} = -\mu_0 \int_{V_{\text{bead}}} (\mathbf{M} \cdot \mathbf{H}) dV \quad (1)$$



Here  $\mathbf{M}$  is the magnetization of the superparamagnetic bead ( $\mathbf{M} = \chi \mathbf{H}$ ),  $\mathbf{H}$  is the total field ( $\mathbf{H} = \mathbf{H}_{\text{DW}} + \mathbf{H}_{\text{ext}}$ ) calculated with OOMMF, including the stray field generated by the ferromagnetic conduit ( $\mathbf{H}_{\text{DW}}$ ), and  $V_{\text{bead}}$  is the particle volume. The bead is modeled as a single magnetic dipole placed in the geometrical centre of the particle, so that Equation 1 becomes:

$$U_{\text{mag}} = -\mu_0 \chi |\mathbf{H}|^2 V_{\text{bead}} \quad (2)$$

The nanoparticle centre is placed at a distance of 540 nm from the nanostructure, in order to take into account the capping layer thickness (40 nm). As illustrated in Figure 3, the potential well minimum is out of the conduit, close to the edge of the corner and along the direction of the external field.

Note that our model neglects the Brownian motion of the particle, which could affect the effective position of the bead on the nanostructure. As a matter of fact, the simulated depth of the magnetic potential well (see Fig. 3) is  $10^4$  times larger than the thermal energy associated to the bead at room temperature, so that the Brownian motion is frozen. To support this argument we estimated the probability (P) of finding a particle at a given distance (d) from its equilibrium position according to the Boltzmann distribution:

$$P(E(d)) = \exp[-(E(d) - E_{\text{eq}}) / K_B T] \quad (3)$$

where  $E(d)$  is the magnetic energy of a superparamagnetic bead (1  $\mu\text{m}$  diameter,  $\chi = 1.43$ ) modeled as a single magnetic dipole.  $E_{\text{eq}}$  is the minimum of the magnetic potential well (see Figure 3) equal to about  $-3.5 \cdot 10^{-17}$  J. From Equation 3, the probability of finding a bead at a distance of 10 nm (the cell size in simulations) from the energy minimum position, along any direction, is lower than  $10^{-5}$ . This confirms that the mean displacement due to Brownian motion is negligible.<sup>[37]</sup>

The experimental data on simultaneous bead transport and detection are presented in **Figure 4**. In panels a-c frames from a video (see Supporting Information) are shown, in which a 1  $\mu\text{m}$  bead in suspension over the magnetic structure is displaced along the conduit, by applying the same sequence of field pulses simulated in Figure 2a-b-c. At the same time, the voltage drop ( $V_{\text{AMR}}$ ) across contacts 2 and 3 is monitored.

Figure 4d-e illustrates  $V_{\text{AMR}}$  as a function of the applied magnetic field ( $H_s$ ) when a single DW is moved towards the sensing corner (Figure 4d) or away from it (Figure 4e). Black and



red curves represent the signals associated to a DW displacement, respectively in absence and presence of a bead bound to it.

The data in Figure 4 show a voltage variation ( $\Delta V_{\text{AMR}}$ ) of about 1.1  $\mu\text{V}$  for each transition, over a baseline of  $\sim 180 \mu\text{V}$ . The percentage resistance variation is 0.6%, lower than the typical AMR of Permalloy in optimized geometries, which is on the order of 2%.<sup>[38,39,40]</sup> This is easily explained by observing the micromagnetic configuration between the sensing electrodes of Figure 2c, which determines  $V_{\text{AMR}}$ . The transverse DW induces only a local magnetization rotation (from parallel to perpendicular to the current direction), while the portions of the conduit closer to the sensing contacts are largely unperturbed and do not contribute to  $\Delta V_{\text{AMR}}$ . This is evident from the simulated maps of conductivity reported in Figure S1 of the Supplementary Information. Note that **the experimental variation of the signal amplitude is in good agreement with simulations.** Indeed, from Figure 2e, the percentage voltage variation when the DW moves away from the measurement corner is 0.8 %.

The critical fields at which the transitions of Figures 4d (DW moving in) and 4e (DW moving out) are observed, correspond to the depinning fields from the previous corner and from that flanked by leads 2 and 3, respectively. **Noteworthy, these fields are the same for displacements towards and away from the corner:  $180 \pm 2$  Oe in absence of bead ( $H_{\text{dep1}}$ ) and  $194 \pm 2$  Oe in presence of 1  $\mu\text{m}$  bead ( $H_{\text{dep2}}$ ), as resulting from the comparison of Fig. 4d and 4e.** The variation of the depinning field value ( $\Delta H_{\text{dep}}$ ) due to the presence of the bead turns out to be  $14 \pm 3$  Oe, well above the experimental error of our measurements, thus allowing for a reliable detection of the bead moving along the conduit. Note that the error of the depinning field measurement ( $\pm 2$  Oe), evaluated as the standard deviation of a set of data acquired in ten different experiments, is only slightly higher than the magnetic field resolution. This is given by the step of the magnetic field in the sweep, set at 1.5 Oe in order to minimize the sweep duration and related thermal drift. These considerations point to the high reproducibility of the measurement of the depinning field, which is determined uniquely by the conduit morphology and is the same, within the experimental error of  $\pm 2$  Oe, for all the corners in the conduit. Indeed, figures 4d and 4e clearly demonstrate through AMR measurements that the depinning fields of two adjacent corners, the one with the contacts and the preceding one, are the same. Moreover, the experimental value of  $\Delta H_{\text{dep}}$  ( $14 \pm 3$  Oe) is in good agreement with the simulated value ( $13.2 \pm 3$  Oe), highlighting that the non-idealities of the experiment (defects in the nanostructures, presence of a liquid over the contacts, Brownian motion of the bead) have a minor impact on the results. Indeed, while  $\Delta V_{\text{AMR}}$  can be influenced by the measurement

conditions (presence of ionic currents, parasitic capacitance, etc...), the DW depinning field represents a robust parameter which is essentially influenced only by the bead position over the conduit. As shown in Figure 3, the strong confinement of the magnetic potential well generated by the DW allows the bead to maintain a precise position with respect to the corner during its motion. This is the reason for the high reproducibility of the depinning field variation induced by the bead, and thus for the reliability of the detection of the bead transit.

To our knowledge these results represent the first demonstration of the real time integrated detection (i.e. with the detector integrated within the very same nanostructure used for transport) of magnetic beads, dragged in liquid by domain walls propagating in magnetic conduits. This is a fundamental step towards the application of DWT technology for particle manipulation. Indeed, previous experiments of bead detection via AMR measurements on square rings and corners were performed in static dry conditions.<sup>[29,30]</sup> In that case, the beads were dispensed in suspension over the chip and then the measurements performed after drying the surface, with the beads collapsed on the chip surface. Here, the beads are moving in a liquid environment during the detection, so that the real-time measurement of sizable and reliable signals is a major achievement.

In order to understand the impact of the out-of-plane position of the bead above the nanostructure, simulations of the depinning field variation ( $\Delta H_{\text{dep}}$ ) as a function of the distance of the bottom of a 1  $\mu\text{m}$  bead from the conduit are presented in **Figure 5a**. In this case, the maximum distance resulting in a detectable depinning field variation is 430 nm, considering a minimum detectable variation of 3 Oe which corresponds to two steps of the magnetic field sweep. To investigate the sensitivity of the detection method, Figure 5b reports the simulated  $\Delta H_{\text{dep}}$  for magnetic moments at saturation of the bead ( $m_s$ ) smaller than that used in our experiments ( $2.45 \cdot 10^{-14} \text{ A} \cdot \text{m}^2$ ), while keeping the bead's bottom surface at a fixed distance of 40 nm from the nanoconduit. To simulate a realistic situation we consider a fixed bead magnetization ( $4.7 \cdot 10^4 \text{ A} \cdot \text{m}^{-1}$ ), corresponding to commercial particles (MICROMOD nanomag®-D), so that the centre of the particle is closer to the surface when decreasing the magnetic moment. It turns out that the minimum detectable  $m_s$  is about  $6.5 \cdot 10^{-15} \text{ A} \cdot \text{m}^2$ , which corresponds to 370 nm-diameter particles. This value has to be compared with previous results, showing that single 130 nm- diameter MICROMOD nanomag®-D can be in principle detected with nanosized corner and square ring structures with capping layer thicknesses below 30 nm.<sup>[29,30]</sup> The lower sensitivity estimated in the present case mainly arises from the different experimental conditions. Here the detection takes place in liquid and in real time, so that the position of the bead on the corner is affected by the presence of the magnetic field. As

discussed above and from our videos (see supplementary material) bead tends to be displaced towards the external edge of the corner upon application of the magnetic field sweep moving the DW and the particle. This is at variance with previous experiments,<sup>[29,30]</sup> performed in a differential way, after drying the chip with nitrogen, where the beads were mainly found close to the centre of the corner, where the effect of the stray field produced by the bead on the corner is maximum.

In order to use the present platform for moving and detecting smaller particles, an optimization of the conduit geometry and particle composition is required. The width of the conduits should be shrunk accordingly to the reduction of the particle size, and beads with higher magnetization should be selected. We estimate that using particles with much higher magnetization than commercial ones (e.g. 2 MA/m for Co particles<sup>[41]</sup>), single particles with 100 nm diameter could be manipulated and detected.

Finally, note that from our experiments and simulations the proposed platform is capable of detecting particles of different size and magnetic moment. Considering the linear relationship  $\Delta H_{\text{dep}}$  vs. particle magnetic moment shown in Fig. 5b and our experimental uncertainty on the depinning field ( $\pm 2$  Oe), it turns out that we could safely distinguish particles belonging to three different batches, with diameter in the 370 nm – 1  $\mu\text{m}$  range. This paves the way to the implementation of an additional active sorting functionality, based on the combination of demultiplexers<sup>[42]</sup> with the zig-zag shaped conduit implementing particle transport and discrimination.

### 3. Conclusion

An on-chip magnetic platform which exploits the same magnetic conduit to manipulate and sense the transit of a single magnetic bead in suspension is presented. By monitoring the AMR signal at a “checkpoint”, we successfully detected, in real-time, the transit of a single 1  $\mu\text{m}$  magnetic particle bound to a domain wall propagating along the conduit.

This platform adds a new functionality to technologies for the on-chip manipulation of magnetic particles: the integration of an electrical feedback on the particle motion. This paves the way to the realization of an integrated close-loop system for accurate manipulation of individual magnetic particles, not requiring the monitoring through microscope and suitable for high-throughput biological experiments or novel microfluidic platforms employing magnetic beads as carriers. Noteworthy, the detection and manipulation are implemented using magnetic fields, so that the method is largely unaffected by the electrical properties of the liquid environment.

## 4. Experimental Section

### *Device Fabrication*

The nanostructure is grown on a SiO<sub>2</sub> (1000 nm)/Si substrate, previously patterned with four Ti (as adhesive layer -3 nm thick-)/Au (20 nm thick) contacts, 100 nm wide in the proximity of magnetic nanostructure (Figure 1b). Electrical contacts have been first deposited by e-beam evaporation and patterned by combining EBL (for the fine extremities) and optical lithography. Then, magnetic zig-zags have been fabricated by electron beam lithography (EBL), e-beam evaporation of Permalloy and lift-off procedure. The nanostructures have been uniformly covered by a protecting capping layer of SiO<sub>2</sub>, 40 nm thick, providing electrical isolation. The top of the device is also equipped by a simple PDMS gasket, sealed to the chip through an O<sub>2</sub> plasma treatment, to contain magnetic particles (see Figure 1b).

### *Magnetic Beads*

Commercial MyOne®-dynabeads (Invitrogen, saturation magnetization  $M_s = 40 \cdot 10^3$  kA/m) superparamagnetic particles with a COOH- surface and a diameter of 1  $\mu$ m have been used to test the device. They have been diluted in water to reach a final concentration of 1  $\mu$ g/ml and dispensed in the PDMS chamber through a micropipette.

### *Electrical Measurements*

The leads (1-2-3-4 in Figure 1c) have been used for 4-wire electrical measurements. The voltage drop across the corner is detected through the inner contacts 2 and 3, using a commercial lock-in amplifier (HF2LI, by Zurich Instruments), while leads 1 and 4 are employed to apply the external AC signal at a frequency of 10-100 kHz. The current injected in the device ranges between 1-4  $\mu$ A (limited by an external resistor  $\sim 100$  k $\Omega$ ) in order not to disrupt the nanostructure by Joule effect. Data are acquired with a bandwidth of 1 Hz and further filtered with a digital notch filter, centered on a periodic interference at 0.1 Hz. The resulting standard deviation of the noise is about 100 nV, allowing a clear detection of the voltage drop variation due to anisotropic magnetoresistance ( $\Delta V_{AMR} \sim 1.1$   $\mu$ V) with a signal-to-noise ratio better than 10.

### *Micromagnetic and transport simulations*

The simulations of the device magnetoresistive response are performed by coupling a micromagnetic solver,<sup>[32,33]</sup> for the determination of the equilibrium magnetic domain configuration, with a magnetotransport model, for the calculation of the current density path and the AMR behavior.<sup>[34,35]</sup> At every applied field step, the micromagnetic solver enables the

computation of the spatial distribution of magnetization vector  $\mathbf{M}$  and effective field  $\mathbf{H}_{eff}$  in the magnetic nanostructure, discretized into a mesh of hexahedra having exchange length size. The time-update of  $\mathbf{M}$  and  $\mathbf{H}_{eff}$ , assumed to be uniform in each hexahedron, is performed by integrating the Landau-Lifshitz-Gilbert equation with a Cayley transform based scheme.<sup>[43]</sup>

In the simulations, the magnetic bead is assumed to be in the superparamagnetic state and approximated as a magnetic dipole, whose stray field interacts with the spatial distribution of the magnetization in the nanostructure. The device-bead interaction is simulated by adding to  $\mathbf{H}_{eff}$  a localized external field, i.e. the stray field produced by the bead, given by

$$\mathbf{H}_{bead} = \frac{1}{4\pi} \left[ \frac{3\mathbf{r}(\mathbf{m}_{bead} \cdot \mathbf{r})}{r^5} - \frac{\mathbf{m}_{bead}}{r^3} \right] \quad (4)$$

In Equation 4,  $\mathbf{m}_{bead}$  is the magnetic moment of the bead, in turn influenced by the stray field generated by the nanostructure magnetization distribution. The dependence of the amplitude of  $\mathbf{m}_{bead}$  on the magnetic field  $H$  (including both the applied external field and the nanostructure stray field) is described by the Langevin function

$$m_{bead}(H) = \frac{M_{S,bead}}{V_{bead}} \left[ \coth\left(\frac{H}{H_0}\right) - \frac{H_0}{H} \right] \quad (5)$$

where  $V_{bead}$  is the volume of the bead,  $M_{S,bead}$  is its saturation magnetization and  $H_0$  is its characteristic field.<sup>[44]</sup>

The micromagnetic modeling is performed assuming for Permalloy a negligible magnetocrystalline anisotropy, a magnetization saturation of 800 kA/m and an exchange constant of 13 pJ/m. The damping parameter is fixed to 0.1, in order to accelerate the reaching of equilibrium states.<sup>[32]</sup>

In the magnetotransport simulations (Figure 2e), the AMR ratio is set at 2%, considering that for Permalloy its magnitude ranges from 2 to 3% at room temperature.<sup>[38,39]</sup> The electrical conductivity  $\sigma_0$  is assumed equal to 3 MS/m (see supplementary information), in agreement with the value found for Permalloy films with similar thickness.<sup>[39]</sup>

The bead parameters  $M_{S,bead}$  and  $\mu_0 H_0$ , obtained by fitting the magnetization curve reported in the manufacturer's Web site with values expressed in emu/g,<sup>[45]</sup> are fixed to 22.5 emu/g and 18 mT, respectively.<sup>[46]</sup> Considering a diameter of 1.05  $\mu\text{m}$  and a density of 1.8 g/cm<sup>3</sup>, a bead saturation magnetic moment of  $2.45 \cdot 10^{-14}$  Am<sup>2</sup> is estimated, corresponding to a saturation magnetization of 40.5 kA/m. The curves shown in Figure 2e are calculated by positioning the bead barycenter at a height of 540 nm above the magnetic conduit, to account for capping layer thickness, and in correspondence of the external edge of the nanostructure corner. This

assumption leads to a reduction of about one third in the variation of the DW depinning field, in comparison to the case with the bead at the corner center.

### Supporting Information

Supporting Information is available from the Wiley Online Library or from the author.

### Acknowledgements

The authors thank M. Leone for his skilful technical support. This work was funded by Fondazione Cariplo via the projects UMANA (2013-0735), by Fondazione Cariplo and Regione Lombardia via the project ESCHIOLO "Early Stage Cancer diagnosis via Highly sensitive Lab-On-chip multi target systems", and by CEN via the project "Forces, mechanisms and pathways involved in the ATR-mediated control of nuclear plasticity in response to mechanical stress" - Rif. EP002.

Received: ((will be filled in by the editorial staff))

Revised: ((will be filled in by the editorial staff))

Published online: ((will be filled in by the editorial staff))

- 
- [1] J. Dobson, *Nat. Nanotechnol.* **2008**, *3*, 139.
- [2] M. Donolato, A. Torti, E. Sogne, N. Kostasheva, M. Deryabina, P. Vavassori, M. F. Hansen, R. Bertacco, *Lab Chip*. **2011**, *11*, 2976-2983.
- [3] J. Kolosnjaj-Tabi, R. Di Corato, L. Lartigue, I. Marangon, P. Guardia, A. K. Silva, N. Luciani, O. Clément, P. Flaud, J. V. Singh, P. Decuzzi, T. Pellegrino, C. Wilhelm, F. Gazeau, *ACS Nano*. **2014**, *27*, 8(5), 4268-83.
- [4] J. Dobson, *Drug development research* **2006**, *67*, 55–60.
- [5] V. C. Martins, F. A. Cardoso, J. Germano, S. Cardoso, L. Sousa, M. Piedade, P. P. Freitas, L. P. Fonseca, *Biosens. Bioelectron.* **2009**, *24*, 2313-2748.
- [6] D. A. Hall, R. S. Gaster, T. Lin, S. J. Osterfeld, S. Han, B. Murmann, S. X. Wang, *Biosens Bioelectron.* **2010**, *15*, 25(9), 2051–2057.
- [7] P. P. Freitas, F. A. Cardoso, V. C. Martins, S. A. M. Martins, J. Loureiro, J. Amaral, R. C. Chaves, S. Cardoso, L. P. Fonseca, A. M. Sebastião, M. Pannetier-Lecoeure, C. Fermone, *Lab Chip*. **2012**, *12*, 546-557.
- [8] T. Deng, G. M. Whitesides, M. Radhakrishnan, G. Zabow, M. Prentiss, *Appl. Phys. Lett.* **2001**, *78*, 1775.
- [9] C. S. Lee, H. Lee, R. M. Westervelt, *Appl. Phys. Lett.* **2001**, *79*, 3308.

- 
- [10] A. H. B. De Vries, B. E. Krenny, R. van Driel, J. S. Kanger, *Biophys. J.* **2005**, 88, 2137.
- [11] B. Yellen, G. Friedman, *Adv. Mater.* **2004**, 16, 111.
- [12] R. S. Conroy, G. Zabow, J. Moreland, A. P. Koretsky, *Appl. Phys. Lett.* **2008**, 93, 203901.
- [13] K. Gunnarsson, P. E. Roy, S. Felton, J. Pihl, P. Svedlindh, H. L. S. Berner, S. Oscarsson, *Adv Mater.* **2005**, 17(14), 1730-1734.
- [14] L. E. Helseth, T. M. Fischer, T. H. Johansen, *Phys. Rev. Lett.* **2003**, 91, 208302.
- [15] P. Tierno, S. V. Reddy, M. G. Roper, T. H. Johansen, T. M. Fisher, *J. Phys. Chem. B.* **2008**, 112, 3833.
- [16] R. Bertacco, M. Donolato, M. Gobbi, M. Cantoni, S. Brivio, D. Petti, P. Vavassori. Manipulation of magnetic particles in conduits for the propagation of domain walls. *PCT/EP2010/000879*, nanoGune Consolider, **2009**, 26, 1494.
- [17] M. Donolato, P. Vavassori, M. Gobbi, M. Deryabina, M. F. Hansen, V. Metlushko, B. Ilic, M. Cantoni, D. Petti, S. Brivio, R. Bertacco, *Adv. Mat.* **2010**, 22, 2706.
- [18] Y. Shao, J. Fu, *Adv. Mat.* **2014**, 26(10), 1494-1533.
- [19] S. Parveen, R. Misra, S. K. Sahoo, *Nanomedicine* **2012**, 10, 1016.
- [20] M. Miller, G. A. Prinz, S. F. Cheng, S. Bounnak, *Appl. Phys. Lett.* **2002**, 81, 2211.
- [21] G. Li, V. Joshi, R. L. White, S. X. Wang, T. X. Kemp, C. Webb, R.W. Davis S. Sun, *J. Appl. Phys.* **2003**, 93, 7557.
- [22] E. Albisetti, D. Petti, M. Cantoni, F. Damin, A. Torti, M. Chiari, R. Bertacco, *Biosens. Bioelectron.* **2013**, 47, 213.
- [23] P. A. Besse, G. Boero, M. Demierre, V. Pott, R. Popovic, *Appl. Phys. Lett.* **2002**, 80, 4199.
- [24] X. Janssen, L. van Ijzendoorn, M. Prins, *Biosens. Bioelectron.* **2007**, 23, 833.
- [25] Z. Jiang, J. Llandro, T. Mitrelias, J. A. C. Bland, *J. Appl. Phys.* **2006**, 99, 08S105.
- [26] R. C. Chaves, D. Bensimon, P. P. Freitas, *J. Appl. Phys.* **2011**, 109, 064702.
- [27] E. Rapoport, D. Montana, G. S. D. Beach, *Lab Chip*, **2012**, 12, 4433–4440.
- [28] M. A. Y. Chang, M. S. C. Lu, *Biosens. Bioelectron.* **2013**, 45, 6–127.
- [29] P. Vavassori, V. Metlushko, B. Ilic, M. Gobbi, M. Donolato, M. Cantoni, R. Bertacco, *Appl. Phys. Lett.* **2008**, 93, 203502.



- 
- [30] M. Donolato, M. Gobbi, P. Vavassori, M. Leone, M. Cantoni, V. Metlushko, B. Ilic, M. Zhang, S. Wang, R. Bertacco, *Nanotechnology* **2009**, *20*, 8550.
- [31] D. M. J. Donahue, 1999 OOMMF User's Guide, Version 1.0. Interagency Report NISTIR **2004**, 6376, 3.
- [32] A. Manzin, O. Bottauscio, *IEEE Trans. Magn.* **2012**, *48*, 2789-2792.
- [33] O. Bottauscio, A. Manzin, *J. Appl. Phys.* **2014**, *115*, 17D122.
- [34] A. Manzin, V. Nabaei, H. Corte-León, O. Kazakova, P. Krzysteczko, H. W. Schumacher, *IEEE Trans. Magn.* **2014**, *50*, 7100204.
- [35] H. Corte-León, V. Nabaei, A. Manzin, J. Fletcher, P. Krzysteczko, H. W. Schumacher, O. Kazakova, *Scientific Reports* **2014**, *4*, 6045.
- [36] E. Martínez, L. López-Díaz, L. Torres, C. J. García-Cervera, *J. Phys. D: Appl. Phys.* **2007**, *40*, 942–948.
- [37] K. V. Ommeringa, J. H. Nieuwenhuis, L. J. van IJzendoorn, B. Koopmans Menno, W. J. Prins, *J. Appl. Phys. Lett.* **2006**, *89*, 142511.
- [38] T. R. McGuire, R. I. Potter, *IEEE Trans. Magn.* **1975**, *11*, 1018-1038.
- [39] E. N. Mitchell, H. B. Haukaas, H. D. Bale, J. B. Streeper, *J. Appl. Phys.* **1964**, *35*, 2604-2608.
- [40] L. K. Bogart, D. Atkinson, *Appl. Phys. Lett.* **2009**, *94*, 042511.
- [41] J. P. Chen, C. M. Sorensen, K. J. Klabunde, *Phys. Rev. B.* **1995**, *51*, 17.
- [42] A. Torti, V. Mondiali, A. Cattoni, M. Donolato, E. Albisetti, A. M. Haghir-Gosnet, Paolo Vavassori, R. Bertacco, *Appl. Phys. Lett.* **2012**, *101*, 142405.
- [43] A. Manzin, O. Bottauscio, *J. Appl. Phys.* **2010**, *108*, 093917.
- [44] J. Lipfert, X. Hao, N. H. Dekker, *Biophys. J.* **2009**, *96*, 5040–5049.
- [45] <http://www.lifetechnologies.com/order/catalog/product/65011?ICID>.
- [46] K. C. Neuman, T. Lionnet, J. F. Allemand, *Annu. Rev. Mater. Res.* **2007**, *37*, 33–67.

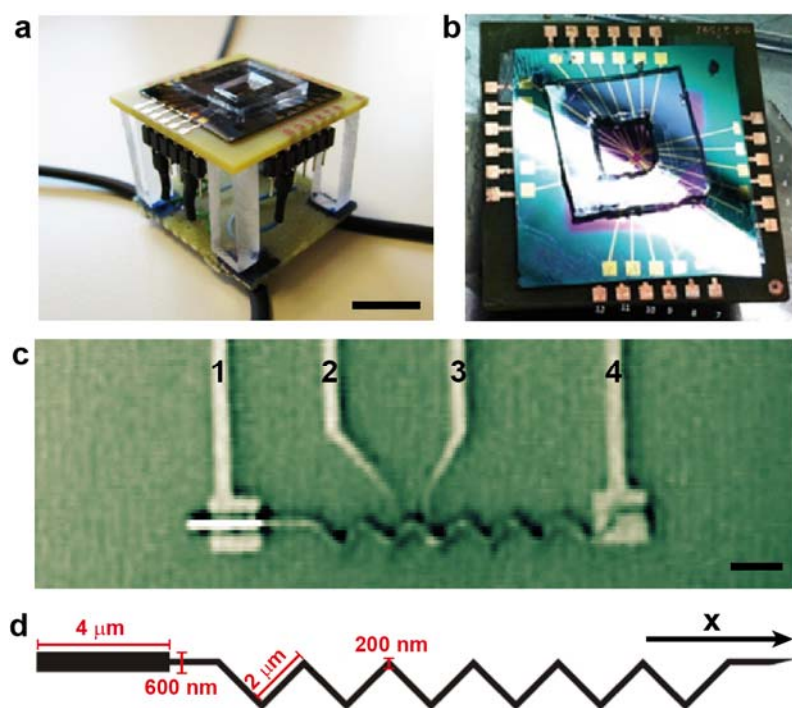


**Figure 1.** (a,b) Pictures of the platform showing the sample stage and the chip, equipped with a PDMS chamber, wire bonded to an interconnection board. (c) Optical microscope image of the device where 1-4 indicate the four leads for AMR measurements. (d) Sketch of magnetic conduit geometry. Scale bars: (a) 2 cm, (c) 4  $\mu\text{m}$ .

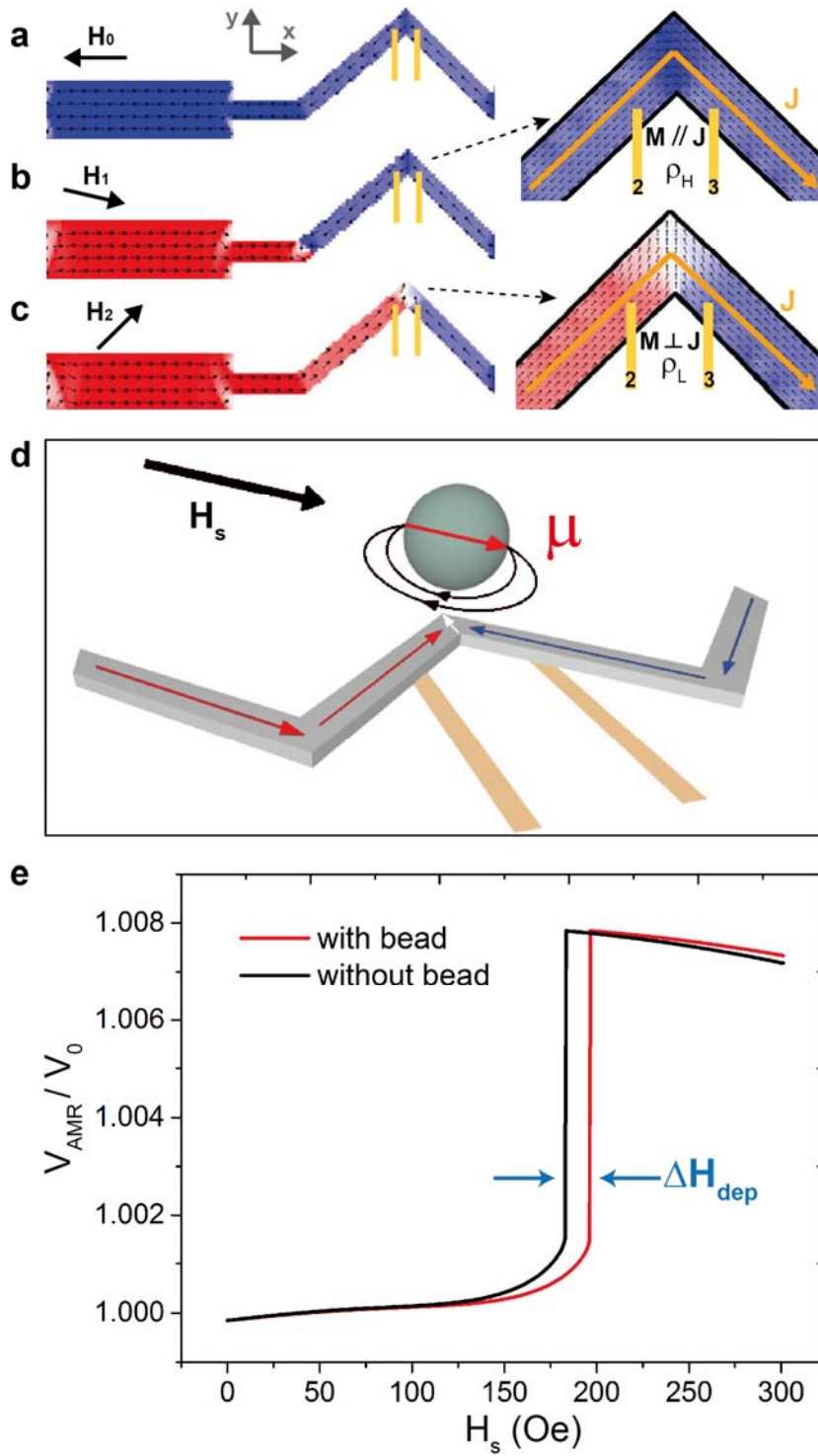


**Figure 2.** (a,b,c) Micromagnetic configuration of the device (calculated with OOMMF) when its magnetization is initialized by a field pulse  $H_0$  (a), a DW is injected applying a field  $H_1$  (b) and the DW is displaced along the corners by a field  $H_2$  (c). On the right, the zoom on the micromagnetic configuration at the measurement corner, in absence or presence of a transverse Néel wall between leads 2-3, is reported. The orange arrow represents the direction of the current injected in the device. (d) Three dimensional sketch of the device with a magnetic bead bound to a DW while sweeping the external magnetic field ( $H_s$ ). (e) Simulation of the AMR voltage drop ( $V_{AMR}$ ) between leads 2-3, normalized to the baseline before the jump ( $V_0$ ), as function of  $H_s$ . Red (black) line refers to a DW depinning with (without) a  $1 \mu\text{m}$  bead trapped 40 nm above the magnetic conduit.

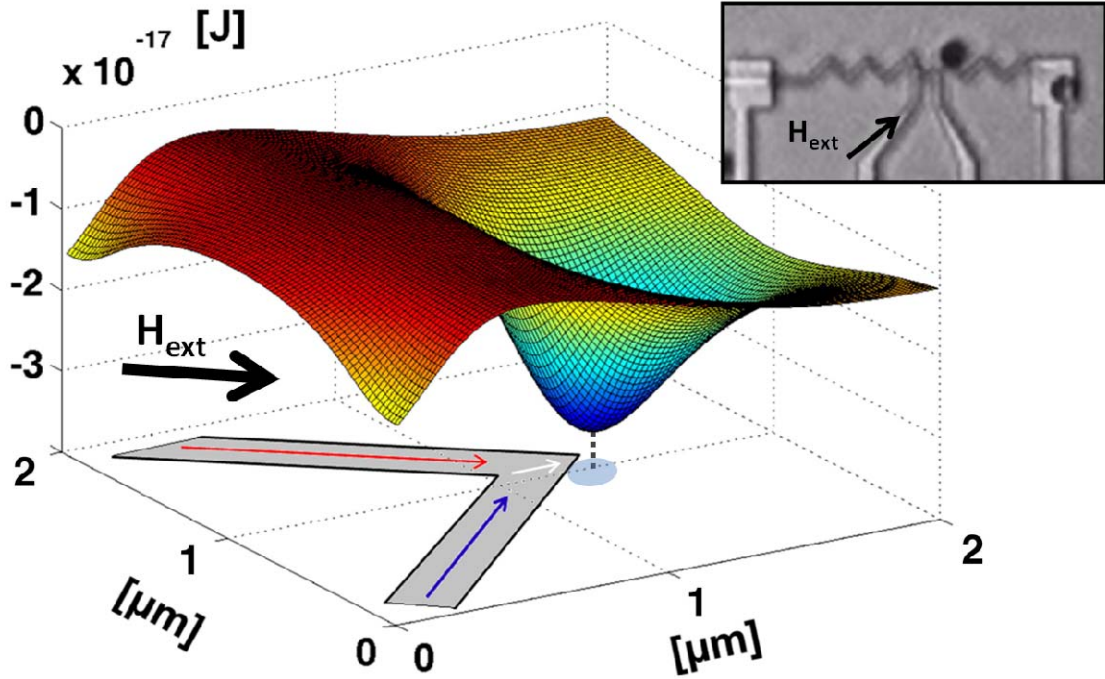


**Figure 3.** Magnetic potential energy well of a superparamagnetic bead (1  $\mu\text{m}$  diameter,  $\chi=1.43$ ) attracted by a transverse domain wall in a zig-zag shaped conduit when an external magnetic field ( $H_{\text{ext}}$ ) of 195 Oe is applied. The bottom of the bead is placed 40 nm above the magnetic conduit. The projection of the potential well minimum on the magnetic conduit plane is located out of the nanostructure corner, close to its edge. In the inset: optical microscopy frame from a video, showing the position of a bead bound to a DW when an external magnetic field ( $H_{\text{ext}}$ ) of 195 Oe is applied.

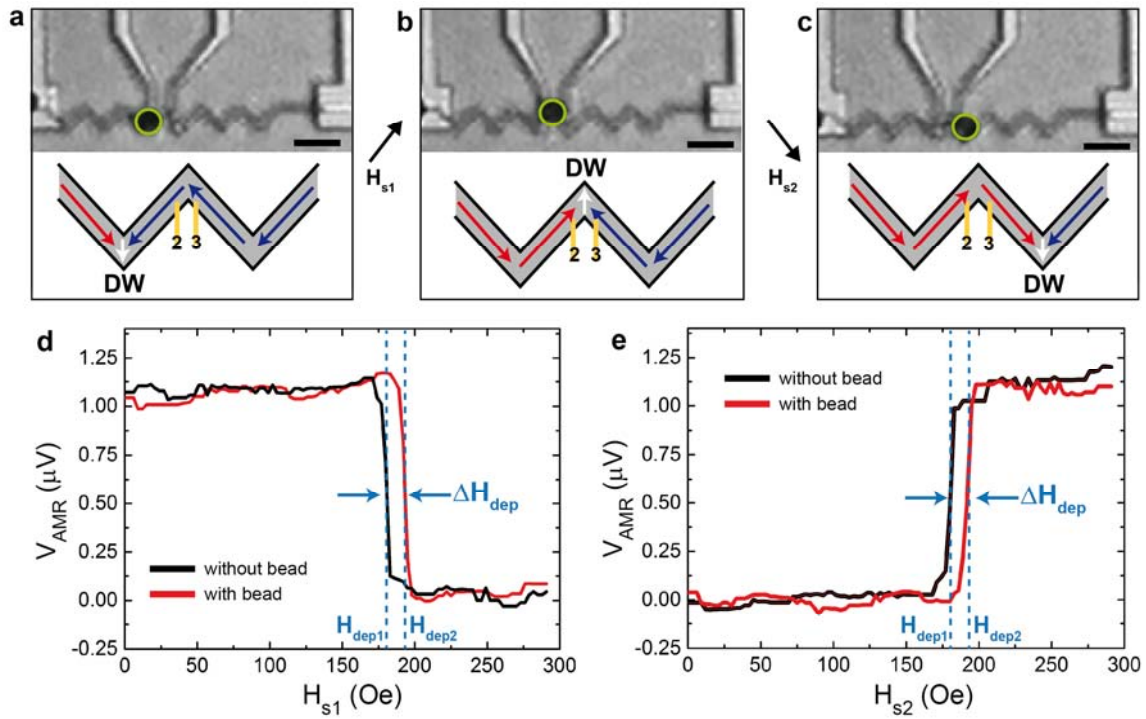


**Figure 4.** (a,b,c) Optical microscope frames from a video on the motion of a single 1  $\mu\text{m}$  bead through the measurement corner, under the application of the external magnetic fields  $H_{s1}$  and  $H_{s2}$ . Scale bars: 5  $\mu\text{m}$ . (d,e) Voltage drop across the corner flanked by leads 2-3 while sweeping  $H_{s1}$  and  $H_{s2}$  from 0 to 300 Oe, after a subtraction of a baseline of  $\sim 180$   $\mu\text{V}$ . A DW is pushed between the electrical contacts (d) or away from them (e) in presence (red curve) or absence (black curve) of a 1  $\mu\text{m}$  magnetic bead bound to it.

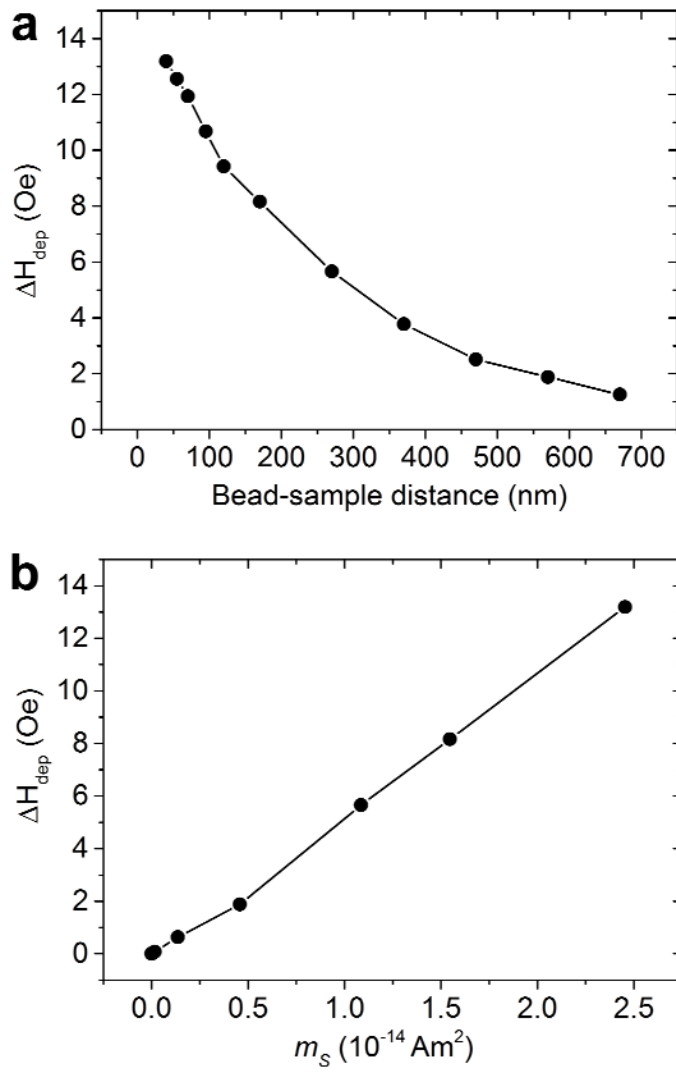


**Figure 5.** (a) Simulation of the depinning field variation ( $\Delta H_{\text{dep}}$ ) as function of the distance between the top of the magnetic conduit and the bottom of  $1\mu\text{m}$  MyOne-Dynabeads ( $m_s = 2.45 \cdot 10^{-14} \text{ Am}^2$ ). (b) Simulation of  $\Delta H_{\text{dep}}$  vs. the bead magnetic moment ( $m_s$ ) for a bead bottom surface at a fixed height of 40 nm above the magnetic conduit.

## Table of contents

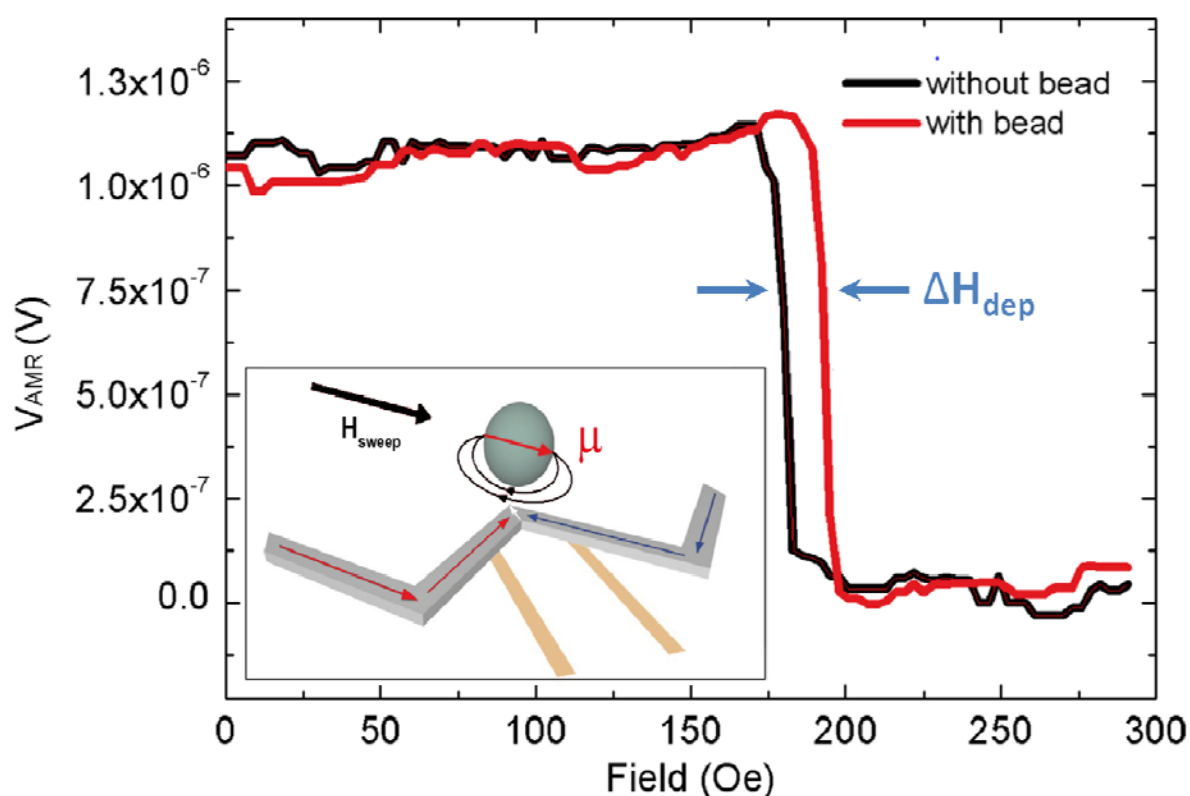
**An innovative on-chip platform suitable to the simultaneous manipulation and integrated detection of a single magnetic bead transit is presented.** The very same magnetic nanostructure is used both to manipulate individual magnetic particles in suspension, bound to magnetic domain walls whose motion is activated by external magnetic fields, and to sense their transit via anisotropic magnetoresistance effect.

**Keyword: Magnetic domain wall tweezers**

M. Monticelli\*, A. Torti, M. Cantoni, D. Petti\*, E. Albisetti, A. Manzin, E. Guerriero, R. Sordan, G. Gervasoni, M. Carminati, G. Ferrari, M. Sampietro and R. Bertacco

**On-chip magnetic platform for single particle manipulation with integrated electrical feedback**

ToC figure (rescale 55 mm x 50 mm)





Copyright WILEY-VCH Verlag GmbH & Co. KGaA, 69469 Weinheim, Germany, 2013.

Supporting Information

### **On-chip magnetic platform for single particle manipulation with integrated electrical feedback**

*Marco Monticelli<sup>\*</sup>, Andrea Torti, Matteo Cantoni, Daniela Petti<sup>\*</sup>, Edoardo Albisetti, Alessandra Manzin, Erica Guerriero, Roman Sordan, Giacomo Gervasoni, Marco Carminati, Giorgio Ferrari, Marco Sampietro and Riccardo Bertacco*

#### *Magnetic simulations by OOMMF*

The magnetic simulations illustrated in Figure 2 a-c and Figure 3 are performed with the software OOMMF (Object Oriented Micro Magnetic Frameworks) [D.M.J Donahue, 1999 OOMMF User's Guide, Version 1.0. interagency Report NISTIR 6376.3, 2004]. The physical space is modeled with a cubic elementary cell of 10 nm x 10 nm x 10 nm. The unit cell dimension is a good trade-off between the requirement of not exceeding the Permalloy exchange length (5.3 nm) [G.S. Abo, T.K. Hong, J. Park, J. Lee, W. Lee, B.C. Choi, "Definition of Magnetic Exchange Length" IEEE Trans. Magnetics, 49(8): 4937-4939, 1979] and limiting the computational time. The damping coefficient is set to the default value of 0.01, which ensures an enough fast convergence to the equilibrium state. Typical parameters for Ni<sub>80</sub>Fe<sub>20</sub> are used: saturation magnetization  $M_s = 860 \cdot 10^3$  A/m, exchange stiffness constant  $A = 1.3 \cdot 10^{-11}$  J/m and no magneto-crystalline anisotropy is considered.

#### *Variation in electrical conductivity due to AMR*

As discussed in the main text, a magnetotransport model [A. Manzin, V. Nabaei, H. Corte-León, O. Kazakova, P. Krzysteczko, H. W. Schumacher. Modeling of anisotropic magnetoresistance properties of permalloy nanostructures, *IEEE Trans. Magn.* 50, **2014**, 7100204] in combination with a micromagnetic solver [O. Bottauscio, A. Manzin. Parallelized micromagnetic solver for the efficient simulation of large patterned magnetic nanostructures. *J. Appl. Phys.* **2014**, 115, 17D122.] are used to simulate the electrical behaviour of a magnetic zig-zag shaped conduit, in order to evaluate its AMR. For the employed geometry, the values of the electrical conductivity in presence and absence of a transverse DW at the measurement corner are illustrated in figure S1. The maximum value for the conductivity is around 3 MS/m when a DW is pinned at the corner and decreases to 2.94 MS/m when the DW is displaced away.

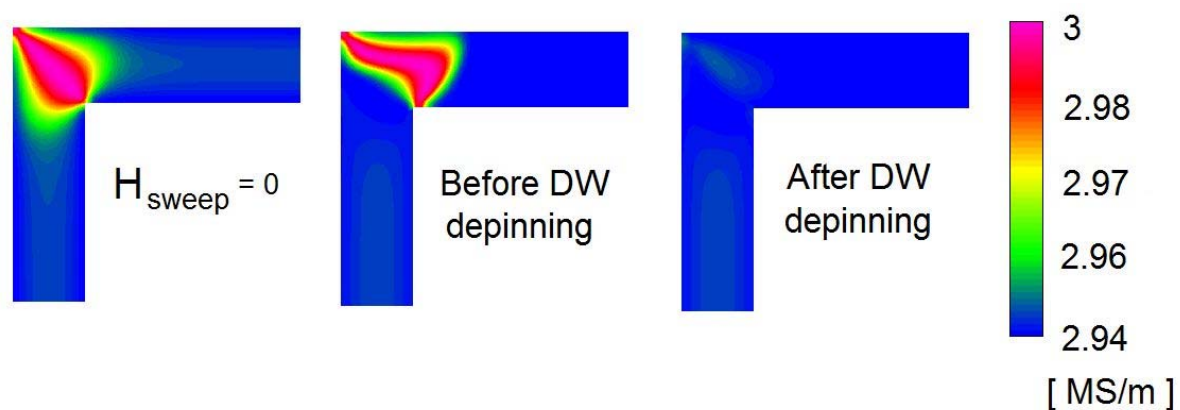


**Figure S1.** Simulated map of the electrical conductivity at the Permalloy corner (200 nm wide and 30 nm thick) at remanence (left), just before (middle) and after (right) the depinning of a transverse DW nucleated at the corner of the nanostructure. The conductivity increases when the DW is located at the corner for the anisotropic magneto resistance effect.